Structural Engineering and Mechanics, Vol. 43, No. 3 (2012) 349-370
DOI: http://dx.doi.org/10.12989/sem.2012.43.3.349

Variable-node element families for mesh connection and adaptive mesh computation

Jae Hyuk Lim[1a], Dongwoo Sohn[2b] and Seyoung Im*[3]

[1]Satellite Structure Department, Korea Aerospace Research Institute (KARI), 169-84 Gwahak-ro,
Yuseong-gu, Daejeon 305-806, Korea
[2]Division of Mechanical and Energy Systems Engineering, College of Engineering,
Korea Maritime University, 727 Taejong-ro, Yeongdo-gu, Busan 606-791, Korea
[3]Department of Mechanical Engineering, Korea Advanced Institute of Science and Technology (KAIST),
Daejeon 305-701, Korea

(Received February 20, 2012, Revised June 19, 2012, Accepted June 26, 2012)

Abstract. Variable-node finite element families, termed $(4+k+l+m+n)$-node elements with an arbitrary number of nodes (k, l, m, and n) on each of their edges, are developed based on the generic point interpolation with special bases having slope discontinuities in two-dimensional domains. They retain the linear interpolation between any two neighboring nodes, and passes the standard patch test when subdomain-wise 2×2 Gauss integration is employed. Their shape functions are automatically generated on the master domain of elements although a certain number of nodes are inserted on their edges. The elements can provide a flexibility to resolve nonmatching mesh problems like mesh connection and adaptive mesh refinement. In the case of adaptive mesh refinement problem, so-called "1-irregular node rule" working as a constraint in performing mesh adaptation is relaxed by adopting the variable-node elements. Through several examples, we show the performance of the variable-node finite elements in terms of accuracy and efficiency.

Keywords: variable-node finite elements; transition elements; nonmatching meshes; adaptive mesh refinement; 1-irregular node rule; mesh connection

1. Introduction

For several decades, finite element method has facilitated straightforward analysis of solids and structures. However, the compatibility requirement imposes some restrictions on the nodal configuration of finite elements, and this is particularly critical when it comes to nonmatching mesh problems. It is far from being trivial to meet the element connectivity in some circumstances, particularly in the case of complex geometries. This class of problems occurs in the interconnection of meshes of substructures comprising an entire structure, in mesh gradation, in adaptive mesh refinement, and so forth.

---

*Corresponding author, Professor, E-mail: sim@kaist.ac.kr
[a] Senior Engineer, E-mail: ljh77@kari.re.kr
[b] Assistant Professor, E-mail: dsohn@hhu.ac.kr

Suppose we construct a large scale finite element mesh composed of numerous substructures, mesh designers create their own parts or substructures independently and then assemble them to create the entire structure. In this circumstance, it is a challenge to treat nonmatching nodes between the interfaces of two neighboring substructures. If this nonmatching problem is not properly treated, the nonmatching nodes may lead to undesirable behaviors because the compatibility of shape functions along the nonmatching interface is not maintained. That is, they may cause solutions not to be converged well.

To resolve the aforementioned issue, various techniques have been proposed, such as two and three layer approaches with Lagrange multipliers (Aminpour *et al.* 1995, Park *et al.* 2002), mortar method (Flemisch *et al.* 2005, Puso 2004), interface element method (Kim 2002, 2008) and improved interface element method or moving least square (MLS)-based variable-node elements (Cho *et al.* 2005, Cho and Im 2006a, b). The two and three layer approaches insert additional conditions on the weak form of governing equations to fulfill the compatibility conditions by introducing Lagrange multipliers. However, it still requires a special treatment such as smoothing or modification of the constraints on the curved interface for optimal convergence (Flemisch *et al.* 2005). The aforementioned approaches (Cho *et al.* 2005, Cho and Im 2006a, b, Kim 2002, 2008) provide a seamless transition between the independent mesh structures, because those shape functions meet the requirement of Kronecker delta condition at nodes, $\phi_I(x_J) = \delta_{IJ}$, by controlling the domain of influence properly. Despite this outstanding feature, rational type shape functions from MLS approximation cause an impediment to application for various problems due to difficulties in numerical integration. Even a high order Gauss integration such as 6 × 6 involves an error as large as one percent in the patch test. In order to enhance the performance of numerical integration, Lim and Im (2007), Lim *et al.* (2007a, b), Kim *et al.* (2008) devised modified MLS-based variable-node elements in two- and three-dimensional frameworks. Their shape functions are generated from MLS approximation, and they reduce to a polynomial type by making a special choice of the bases and by controlling the domain of influence of each node. Applications for various nonmatching mesh problems were successful even with a lower order Gauss integration, such as 2 × 2 per subdomain for bilinear polynomial bases. However, they are allowed to have extra nodes only either along the ξ-direction or along the η-direction on the parental domain. For a remedy, special integration schemes like smoothed nodal integrations (Lim *et al.* 2010, Liu *et al.* 2007, Nguyen-Thoi *et al.* 2011, Sohn *et al.* 2012) are needed.

The objective of the paper is to report on variable-node element families, termed $(4+k+l+m+n)$-node elements, which allow an arbitrary number of nodes (k, l, m, and n) along each of the two coordinate directions ξ and η using the point interpolation. For numerical integration, they only require a 2 × 2 Gauss integration per subdomain comprising one element, which have advantages over aforementioned approaches (Cho *et al.* 2005, Cho and Im 2006a, b) in terms of computation time and accuracy. In addition, they have a generality with respect to the number of side nodes (k, l, m, and n) and require a lower order Gauss integration in contrast to other approaches (Kim *et al.* 2008, Lim and Im 2007, Lim *et al.* 2007a, b). The conceptual idea of the $(4+k+l+m+n)$-node elements using the point interpolation is briefly discussed by Lim *et al.* (2010) for the purpose of comparison with variable-node finite elements combined with smoothed nodal integration. However, their theoretical background and the characteristics of shape functions have never been explained in any literature in detail.

The other goal of the paper is to investigate its performance and show applications with the emphasis on the relaxing the 1-irregular node rule, a bothersome hurdle, in adaptive mesh refinement (Choi and Lee 1993, 1996, Choi *et al*. 2004, Choi and Park 1992, Lo *et al*. 2006, 2010, Wu *et al*. 2008, Zienkiewicz and Zhu 1987).

The remainder of this paper is organized as follows: We first explain a scheme of mesh connection and adaptive mesh refinement with the aid of variable-node finite element families in Section 2. This is followed by the formulation of the variable-node finite element families employing the point interpolation and a detail investigation on the characteristics of shape functions in Section 3. In addition, we provide some numerical examples to demonstrate the effectiveness of this methodology through examples of patch test, mesh connection, and adaptive mesh refinement. Finally, we close with some concluding remarks.

2. Mesh connection and adaptive mesh refinement using variable-node finite element families

For two nonmatching meshes as shown in Fig. 1, suppose two mesh designers construct independent meshes of the two substructures on Ω_1 and Ω_2, respectively. This, in general, results in nonmatching meshes along the mesh interface region $\Omega_1 \cap \Omega_2$, in which the compatibility of shape functions is not assured. To circumvent this situation, additional nodes are inserted on the neighboring elements whenever nonmatching nodes appear, and then replace the elements having more than four nodes with the variable-node elements along the interface, as seen in Fig. 1. Finally, fully continuous mesh interface can be achieved by our suggested approach. We may further extend this concept to any problems associated with nonmatching mesh situations such as contact (Kim *et al*. 2008), multi-level analysis of crack propagation (Sohn *et al*. 2011), mesh gradation (Lim and Im 2007) and so forth.

In the case of adaptive mesh refinement (Zienkiewicz and Zhu 1987), there are several ways to

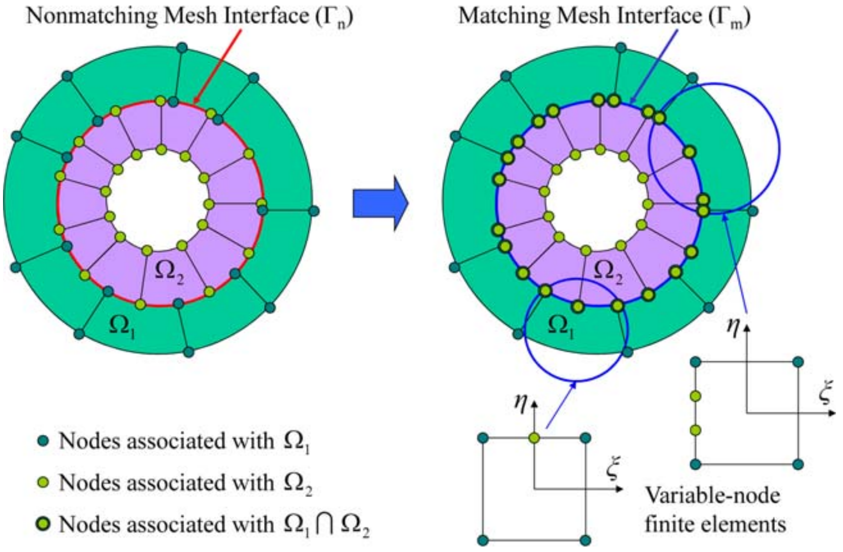

Fig. 1 Transformation from nonmatching meshes to matching meshes with the aid of the variable-node finite elements

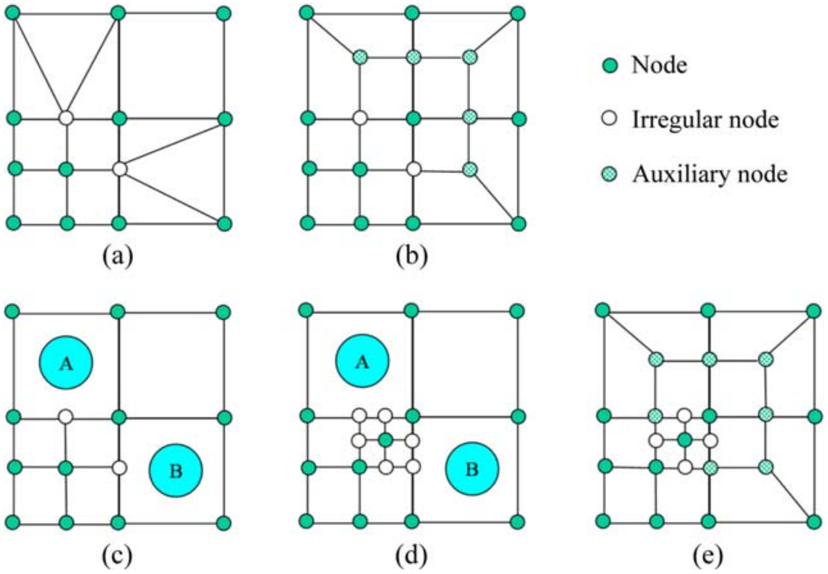

Fig. 2 Various ways of connecting nonmatching meshes and irregular nodes: (a) three-node element-based mesh refinement; (b) four-node element-based mesh refinement; (c) one irregular node; (d) two irregular nodes; (e) two irregular nodes handling by splitting the neighboring elements A and B

treat nonmatching nodes or irregular nodes, as seen in Figs. 2(a)-(c). In Fig. 2(a), one irregular node is connected by splitting its neighboring elements into three triangle elements. In Fig. 2(b), the refinement is achieved by generating distorted three quadrilateral elements. However, this kind of refinement is not recommended because they not only require an additional remeshing procedure but also lose the mesh quality. Without remeshing, we may connect two different meshes by imposing approximate constraints such as a penalty parameter whereby the displacement of a mid-node or an irregular node is equal to a weighted average value of the displacements at the two neighboring vertex nodes, as depicted in Fig. 2(c). However, this approximation is tolerable only for one irregular node because of the worsening accuracy in the case of more than one irregular node. This requirement is called the 1-irregular node rule (Choi and Lee 1993, 1996, Choi *et al*. 2004, Choi and Park 1992, Lo *et al*. 2006, 2010, Wu *et al*. 2008, Zienkiewicz and Zhu 1987). In order to increase the accuracy of mesh connection, transition elements have been used in adaptive mesh refinement (Choi and Lee 1993, 1996, Choi *et al*. 2004, Choi and Park 1992), and their enhancement combined with hybrid stress theory was also reported (Lo *et al*. 2006, 2010, Wu *et al*. 2008). However, they were still governed by the 1-irregular node rule because their transition elements can accommodate only 1-irregular nodes. When the element is refined once more as shown in Fig. 2(d), two or more irregular nodes are generated on an element-edge. To follow the 1-irregular node rule in this case, we should split the adjacent elements A and B in Fig. 2(d), as shown in Fig. 2(e). In this circumstance, it is worthwhile to apply the variable-node element families for coupling of nonmatching meshes in adaptive mesh refinement. By replacing the elements A and B in Fig. 2(d) with the variable-node elements which contain two irregular nodes on an element-edge, the mesh connection is straightforwardly achieved without the additional refinement in Fig. 2(e).

3. Variable-node finite element families using the point interpolation

In this section, we explain how to derive the shape functions of variable-node finite element families from the point interpolation, using a set of bases having the slope discontinuity. As a first step toward this, we first briefly review a four-node bilinear finite element and other variable-node elements, which were introduced by Gupta (1978) and Hughes (1989), based on the point interpolation.

Let $\mathbf{u}(\boldsymbol{\xi})$ be a two-dimensional vector field, and $u_\alpha\,(\alpha = 1, 2)$ its two components interchangeably denoted by (u, v). The independent variable $\boldsymbol{\xi}$ indicates the master coordinate $(\xi_1,\ \xi_2)$, interchangeably indicated by $(\xi,\ \eta)$ for convenience. Considering the approximated displacement $\mathbf{u}^h(\boldsymbol{\xi})$ for $\mathbf{u}(\boldsymbol{\xi})$ by the point interpolation with base-polynomials of which the number is N_B, $\mathbf{u}^h(\boldsymbol{\xi})$ is then given as follows

$$\mathbf{u}^h(\boldsymbol{\xi}) = \sum_{I=1}^{N_P} \boldsymbol{\varphi}_I(\boldsymbol{\xi})\mathbf{u}_I = \mathbf{a}^T\mathbf{p}(\boldsymbol{\xi}) \tag{1}$$

$$\boldsymbol{\varphi}_I(\boldsymbol{\xi}) = \begin{bmatrix} \phi_I & 0 \\ 0 & \phi_I \end{bmatrix} \tag{2}$$

$$\mathbf{u}_I = [u_I, v_I]^T \tag{3}$$

where $\mathbf{a}^T$ is a $2 \times N_B$ matrix of the unknown coefficients and $\mathbf{p}(\boldsymbol{\xi})$ is a $N_B \times 1$ column vector of the polynomial basis. Furthermore, $\phi_I(\boldsymbol{\xi})$ is a shape function associated with node I, and $\boldsymbol{\varphi}_I(\boldsymbol{\xi})$ is a 2×2 shape function matrix and $\mathbf{u}_I$ is a nodal variable of 2×1 column vector. Let N_P indicate the number of sampling points in the point interpolation. In the framework of the point interpolation, N_P is identical to N_B. The polynomial basis can be given as

$$\mathbf{p}(\boldsymbol{\xi}) = [1, \xi, \eta, \xi\eta, \xi^2, \eta^2, \ldots]^T \tag{4}$$

Every shape function from the point interpolation is associated with its own node, being equal to 1 at its associated node and to 0 at all the remaining nodes. Thus, the Kronecker delta property is fulfilled in the point interpolation. From the point interpolation, it follows that

$$\mathbf{u}^h(\boldsymbol{\xi}) = \mathbf{a}^T\mathbf{p}(\boldsymbol{\xi}) = \mathbf{U}^T\mathbf{P}^{-1}\mathbf{p}(\boldsymbol{\xi}) \tag{5}$$

where $\mathbf{P} = \mathbf{P}(\boldsymbol{\xi}_I)$ and $\mathbf{U}$ are given as

$$\mathbf{P} = \begin{bmatrix} 1 & 1 & 1 & \ldots & 1 \\ \xi_1 & \xi_2 & \xi_3 & \cdots & \xi_{N_P} \\ \eta_1 & \eta_2 & \eta_3 & \cdots & \eta_{N_P} \\ \xi_1\eta_1 & \xi_2\eta_2 & \xi_3\eta_3 & \cdots & \xi_{N_P}\eta_{N_P} \\ \xi_1^2 & \xi_2^2 & \xi_3^2 & \cdots & \xi_{N_P}^2 \\ \eta_1^2 & \eta_2^2 & \eta_3^2 & \cdots & \eta_{N_P}^2 \\ \vdots & \vdots & \vdots & \vdots & \vdots \end{bmatrix}_{N_P \times N_P}$$

$$\mathbf{U}^T = \begin{bmatrix} u_1 & u_2 & u_3 & \dots & u_{N_P} \\ v_1 & v_2 & v_3 & \dots & v_{N_P} \end{bmatrix}_{2 \times N_P}$$

For the four-node bilinear interpolation, we only consider the bilinear basis, $\mathbf{p}(\xi) = [1, \xi, \eta, \xi\eta]^T$, and the nodes at the master domain as seen in Fig. 3(a). The shape functions are then given as follows

$$\mathbf{N}(\xi) = [\phi_1(\xi), \phi_2(\xi), \phi_3(\xi), \phi_4(\xi)]^T$$
$$= \left[\frac{1}{4}(1-\xi)(1-\eta), \frac{1}{4}(1+\xi)(1-\eta), \frac{1}{4}(1+\xi)(1+\eta), \frac{1}{4}(1-\xi)(1+\eta)\right]^T \tag{6}$$

Similarly, we can also obtain two well-known kinds of five-node transition elements reported by Gupta (1978) and Hughes (1989). When the fifth node is inserted at the middle of the upper side of a four-node element, an extra special basis should be added to meet the point interpolation. As to what basis is chosen for the interpolation, it depends upon the type of interpolation required on the element-edges. For example, if a quadratic interpolation along the top side is desired while a linear interpolation is needed along the bottom side, $\xi^2(\eta + 1)$ is chosen as an additional special basis (see

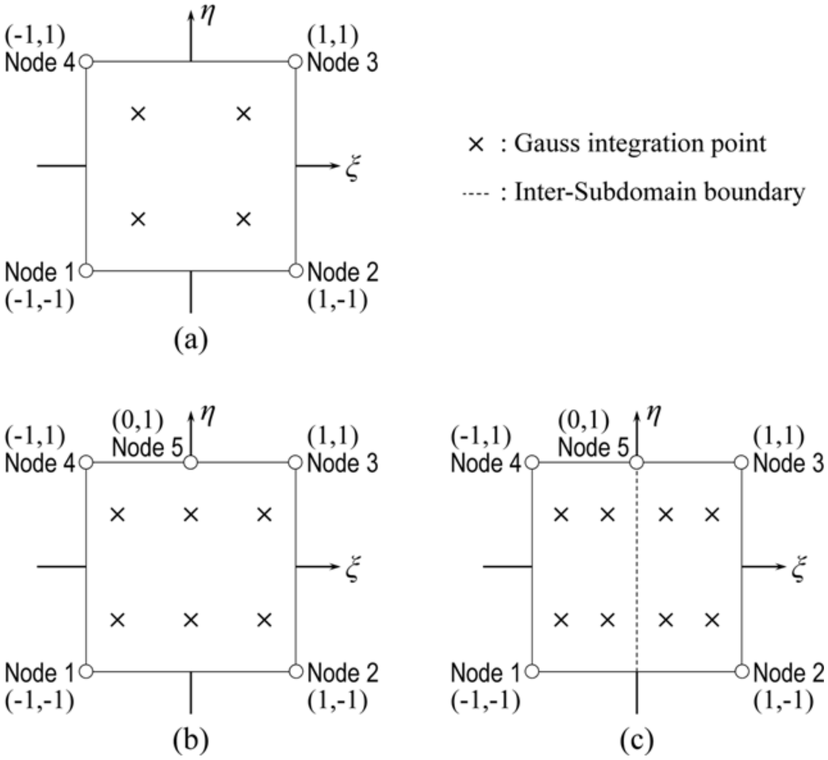

Fig. 3 Master domains of quadrilateral elements: (a) a four-node bilinear element, (b) a five-node element with a quadratic interpolation at the upper edge, (c) a five-node element with a linear interpolation at the upper edge

Fig. 3(b)). This basis reduces to ξ^2 at $\eta = 1$ while it disappears at $\eta = -1$. The shape functions are then derived in a straightforward manner, as described in Eq. (5), and yield the following result, which was reported by Gupta (1978).

$$\begin{aligned}\mathbf{N}(\xi) &= [\phi_1(\xi), \phi_2(\xi), \phi_3(\xi), \phi_4(\xi), \phi_5(\xi)]^T \\ &= \Big[\frac{1}{4}(1-\xi)(1-\eta), \frac{1}{4}(1+\xi)(1-\eta), \frac{1}{4}(1+\xi)(1+\eta) - \frac{1}{4}(1-\xi^2)(1+\eta) \\ &\quad \frac{1}{4}(1-\xi)(1+\eta) - \frac{1}{4}(1-\xi^2)(1+\eta), \frac{1}{2}(1-\xi^2)(1+\eta)\Big]^T \end{aligned} \tag{7}$$

For numerical integration, the 3 × 2 Gauss integration is sufficient at the master domain, as depicted in Fig. 3(b). In the same way, we derive a bilinear five-node element in Fig. 3(c). We use a special basis of $|\xi|(\eta + 1)$ having the slope discontinuity instead of $\xi^2(\eta + 1)$ for linear interpolation on the upper side, and easily obtain the shape functions below

$$\begin{aligned}\mathbf{N}(\xi) &= [\phi_1(\xi), \phi_2(\xi), \phi_3(\xi), \phi_4(\xi), \phi_5(\xi)]^T \\ &= \Big[\frac{1}{4}(1-\xi)(1-\eta), \frac{1}{4}(1+\xi)(1-\eta), \frac{1}{4}(1+\xi)(1+\eta) - \frac{1}{4}(1-|\xi|)(1+\eta) \\ &\quad \frac{1}{4}(1-\xi)(1+\eta) - \frac{1}{4}(1-|\xi|)(1+\eta), \frac{1}{2}(1-|\xi|)(1+\eta)\Big]^T \end{aligned} \tag{8}$$

From Eq. (8), we confirm that the interpolation along the upper side in Fig. 3(c) is comprised of two linear-interpolations between nodes 4 and 5, and between nodes 5 and 3, and all element boundaries retain a linear interpolation between neighboring two nodes. However, it is necessary to

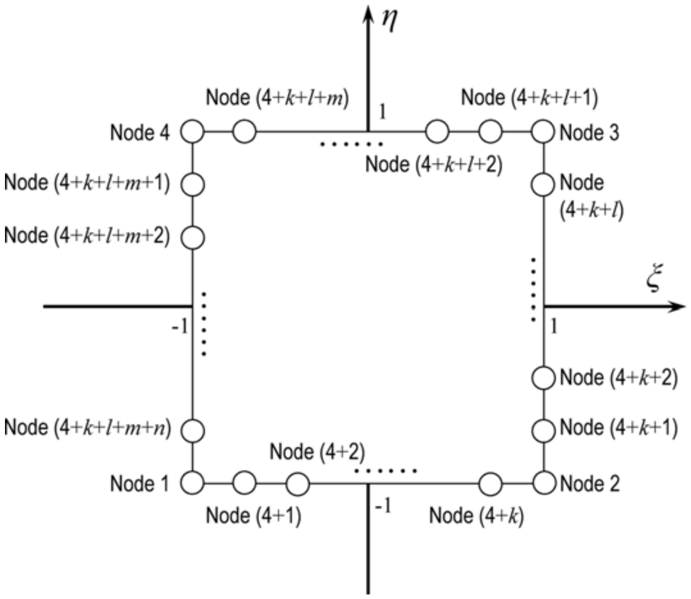

Fig. 4 The master element of $(4 + k + l + m + n)$-node finite elements

modify the numerical integration due to the slope discontinuity of the special basis $|\xi|(\eta+1)$. To overcome the slope discontinuity in the numerical integration, the 2×2 Gauss integration per subdomain is used because the shape functions still show bilinear interpolation within a subdomain despite the slope discontinuity at the element level.

The slope discontinuous basis at node 5 along the upper side and the vanishing of the basis along the lower boundary are extremely useful in constructing new variable-node finite elements. With this concept, a linear variable-node element, termed the $(4+k+l+m+n)$-node element, could be generalized to accommodate an arbitrary placement of k additional nodes on the bottom edge of a four-node element, l additional nodes on the right edge, m additional nodes on the top edge, and n additional node on the left edge, as shown in Fig. 4. Consider a set of special bases given as

$$|\xi-\xi_i|(\eta-1),|\xi-\xi_i|(\eta+1),|\eta-\eta_i|(\xi-1),|\eta-\eta_i|(\xi+1) \tag{9}$$

The first base function retains a slope discontinuity along the bottom side of the element, but this slope discontinuity disappears on the top side, $\eta=1$. In a similar manner, the second one has the slope discontinuity along the top side of the element while it disappears on the bottom side. The third and the fourth base function possess the slope discontinuity along each of the left and the right side of the element, respectively.

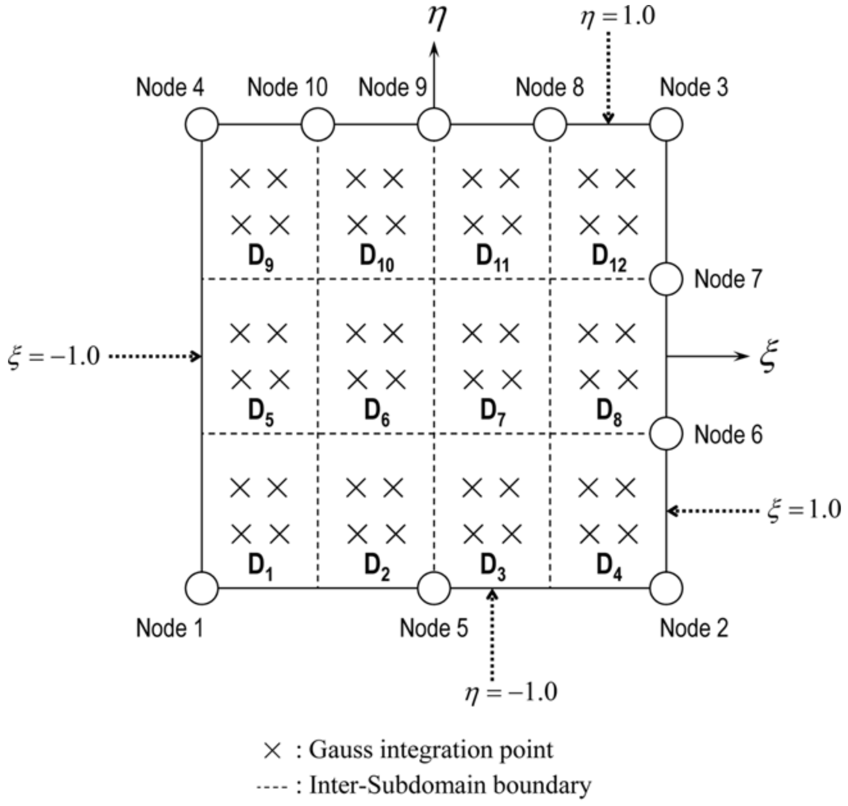

Fig. 5 A $(4+k+l+m+n)$-node finite element with linear interpolation on the boundary: $k=1$, $l=2$, $m=3$, $n=0$

As a simple example, we assume $k = 1$, $l = 2$, $m = 3$, and $n = 0$, as described in Fig. 5. It has total ten nodes in the element domain. The special bases adopted for representing the slope discontinuity are $|\xi + 0|(\eta - 1)$, $|\eta + 1/3|(\xi + 1)$, $|\eta - 1/3|(\xi + 1)$, $|\xi - 1/2|(\eta + 1)$, $|\xi - 0|(\eta + 1)$, and $|\xi + 1/2|(\eta + 1)$ for node 5, node 6, node 7, node 8, node 9, and node 10, respectively with equally spacing subdomain. These shape functions are plotted in Fig. 6, which shows that all the shape functions satisfy the continuity and compatibility at the element boundary.

The desirable properties of finite element shape functions may include the followings: (1) partition of unity ($\sum_{I=1}^{N_P} \phi_I(\xi) = 1.0$); (2) Kronecker delta condition ($\phi_I(\mathbf{x}_J) = \delta_{IJ}$); (3) linear completeness at the element domain ($\sum_{I=1}^{N_P} \phi_I(\xi)\mathbf{x}_I = \mathbf{x}$); (4) at least piecewise linear interpolation between two neighboring nodes at all element boundaries; (5) non-negativeness: ($0 \le \phi_I(\xi)$); and (6) sufficient smoothness in the element interior.

Polygon elements of linear-interpolation type which include Wachspress basis function (Wachspress 1975) and mean-value coordinates (Floater 2003) meet the aforementioned conditions. Our variable-node element meets the first four conditions above but do not guarantee the fifth condition, which has relevance to the discrete maximum principle (Christie and Hall 1984, Varga 1966). As illustrated from Fig. 6, two of the present shape functions at corner nodes, ϕ_2 and ϕ_3, have negative value at local region. This characteristic of shape function is also noticed in

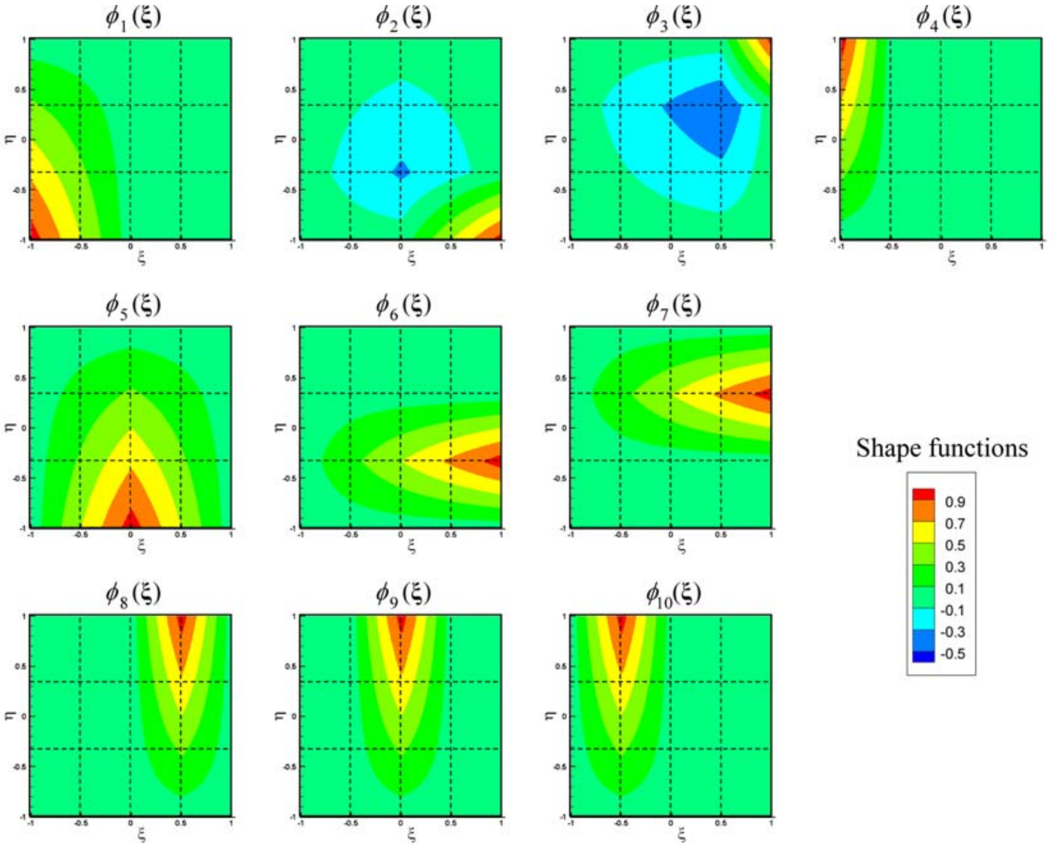

Fig. 6 Shape functions of a $(4 + k + l + m + n)$-node element in the case of $k = 1$, $l = 2$, $m = 3$, $n = 0$: $\phi_1(\xi)$ through $\phi_{10}(\xi)$

conventional eight- and nine-node quadratic elements. Regarding the sixth condition, the present variable-node elements retain C^1 smoothness in the interior of the element except the inner boundaries located in the slope discontinuity due to absolute value of the bases in Eq. (9). For the inner boundaries, C^0 smoothness is satisfied. This means no difficulties when the numerical integration is carried out subdomain-wisely, as indicated in Fig. 5. The 2 × 2 Gauss integration per subdomain is a sufficient integration order, because the shape functions still show bilinear interpolation at each subdomain in the same way as the aforementioned transition element (Hughes 1989). Note that the shape functions of the $(4+k+l+m+n)$-node elements with an arbitrary number of k, l, m and n on the master elements can be automatically generated with the slope discontinuity bases in Eq. (9) without losing the continuity and compatibility at the element boundary.

4. Numerical examples

To demonstrate the performance of the proposed variable-node finite element families, some benchmark problems are treated in this section. In the first two examples, we deal with mesh connection problems including the patch test. Subsequently, in the last two examples, we demonstrate how to efficiently apply the variable-node elements for adaptive mesh refinement. In all examples, the conventional isoparametric mapping is used.

4.1 Mesh connection using variable-node element families

4.1.1 Patch test

For the series of patch tests, we prepared a patch as shown in Fig. 7. The patch is constructed by one highly distorted $(4+k+l+m+n)$-node finite element on Ω_2 and many 4-node quadrilateral elements on Ω_1. We impose proper boundary conditions to remove rigid body modes and realize a simple tension state under plane stress condition. We use the same material properties for both of

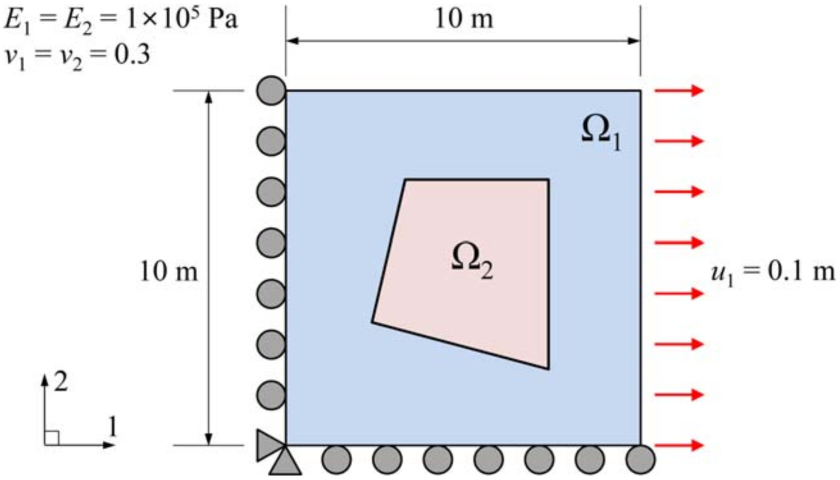

Fig. 7 Geometry and boundary conditions for the patch test

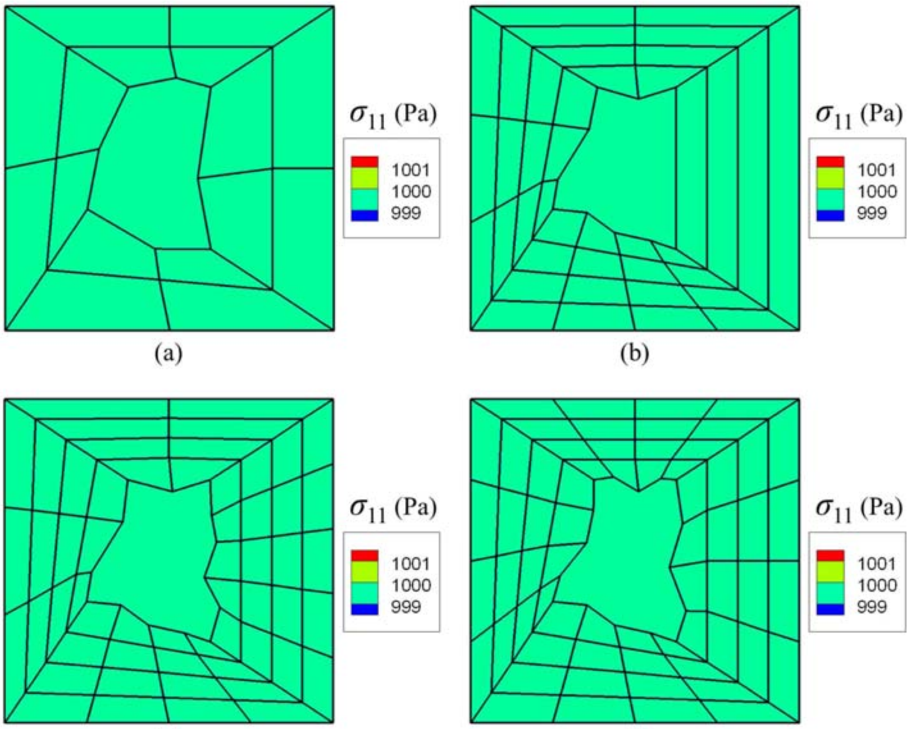

(a) (b)

(c) (d)

Fig. 8 σ_{11} contour plots of the patch with a $(4 + k + l + m + n)$-node element in the case of: (a) ($k = 1$, $l = 1$, $m = 1$, $n = 1$); (b) ($k = 3$, $l = 0$, $m = 1$, $n = 2$); (c) ($k = 3$, $l = 4$, $m = 1$, $n = 2$); (d) ($k = 3$, $l = 3$, $m = 3$, $n = 3$)

Table 1 Relative error in energy norm of patch tests with various irregular nodes

Test case	Relative Error in Energy norm
(a) $k = 1$, $l = 1$, $m = 1$, $n = 1$	1.39×10^{-15}
(b) $k = 3$, $l = 0$, $m = 1$, $n = 2$	4.47×10^{-15}
(c) $k = 3$, $l = 4$, $m = 1$, $n = 2$	2.63×10^{-15}
(d) $k = 3$, $l = 3$, $m = 3$, $n = 3$	4.04×10^{-15}

Ω_1 and Ω_2; Young's modulus and Poisson's ratio are 1×10^5 Pa and 0.3, respectively. To demonstrate the generality and robustness of the proposed elements, we consider a set of different numbers of nodes at every side of the $(4 + k + l + m + n)$-node element: $(k, l, m, n) = (1, 1, 1, 1)$, $(3, 0, 1, 2)$, $(3, 4, 1, 2)$, and $(3, 3, 3, 3)$. As plotted in Fig. 8, we confirm that all patches reproduce the constant tension state regardless of the number of inserted nodes. It is noted that the relative error in energy norm of all mesh configurations are about $O(10^{-15})$, as summarized in Table 1, which is equivalent to the machine epsilon of 32 bit personal computer.

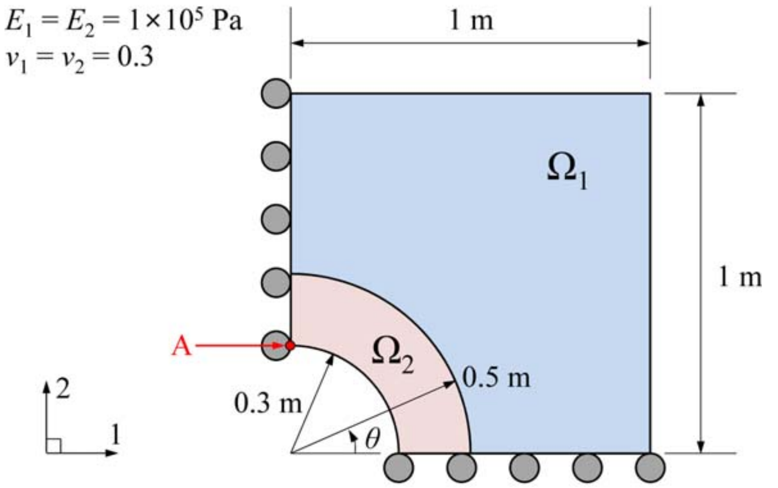

Fig. 9 Geometry and boundary conditions of an infinite block including a hole

4.1.2 An infinite plane-strain block with a hole under tension

For the second example, we choose an infinite two-dimensional body including a hole. We only use one quarter of the model by imposing proper boundary conditions, as depicted in Fig. 9. The block has the dimension of 1 m × 1 m, and has a hole with radius of 0.3 m. To capture stress concentration, we take subdivision on Ω_2 and replace those elements of Ω_1 that are neighboring Ω_2 along the interface by the $(4 + k + l + m + n)$-node elements (see Figs. 9 and 10(b), (d), (f)). The block is under plane strain condition and is subjected to uniform tension of $\sigma_0 = 1$ Pa in the horizontal direction. The Young's modulus and Poisson ratio are 10^6 Pa and 0.3, respectively. To realize the infinite body state in a finite body, we calculate exact nodal forces by integrating exact stress distributions for the infinite body, given by Eq. (10), with the 12th order Gauss integration along the boundary, and impose these forces on the outer boundary (Timoshenko and Goodier 1970).

$$\sigma_{11}(r, \theta) = \sigma_0\left(1 - \frac{a^2}{r^2}\left(\frac{3}{2}\cos 2\theta + \cos 4\theta\right) + \frac{3}{2}\frac{a^4}{r^4}\cos 4\theta\right)$$

$$\sigma_{22}(r, \theta) = \sigma_0\left(-\frac{a^2}{r^2}\left(\frac{1}{2}\cos 2\theta - \cos 4\theta\right) - \frac{3}{2}\frac{a^4}{r^4}\cos 4\theta\right)$$

$$\sigma_{12}(r, \theta) = \sigma_0\left(-\frac{a^2}{r^2}\left(\frac{1}{2}\sin 2\theta + \sin 4\theta\right) + \frac{3}{2}\frac{a^4}{r^4}\sin 4\theta\right) \qquad (10)$$

The stress contours of σ_{11} are described in Fig. 10, wherein conventional meshes without any irregular nodes (Figs. 10(a), (c), (e)) and locally refined meshes with the irregular nodes accommodated in the variable-node elements (Figs. 10(b), (d), (f)) are shown for the comparison of their performances. Fig. 11 shows the relative error in energy norm on Ω_2 and the maximum tensile stress σ_{11} at the Gauss point nearest to the left lower vertex "A" (see Fig. 9) with respect to the

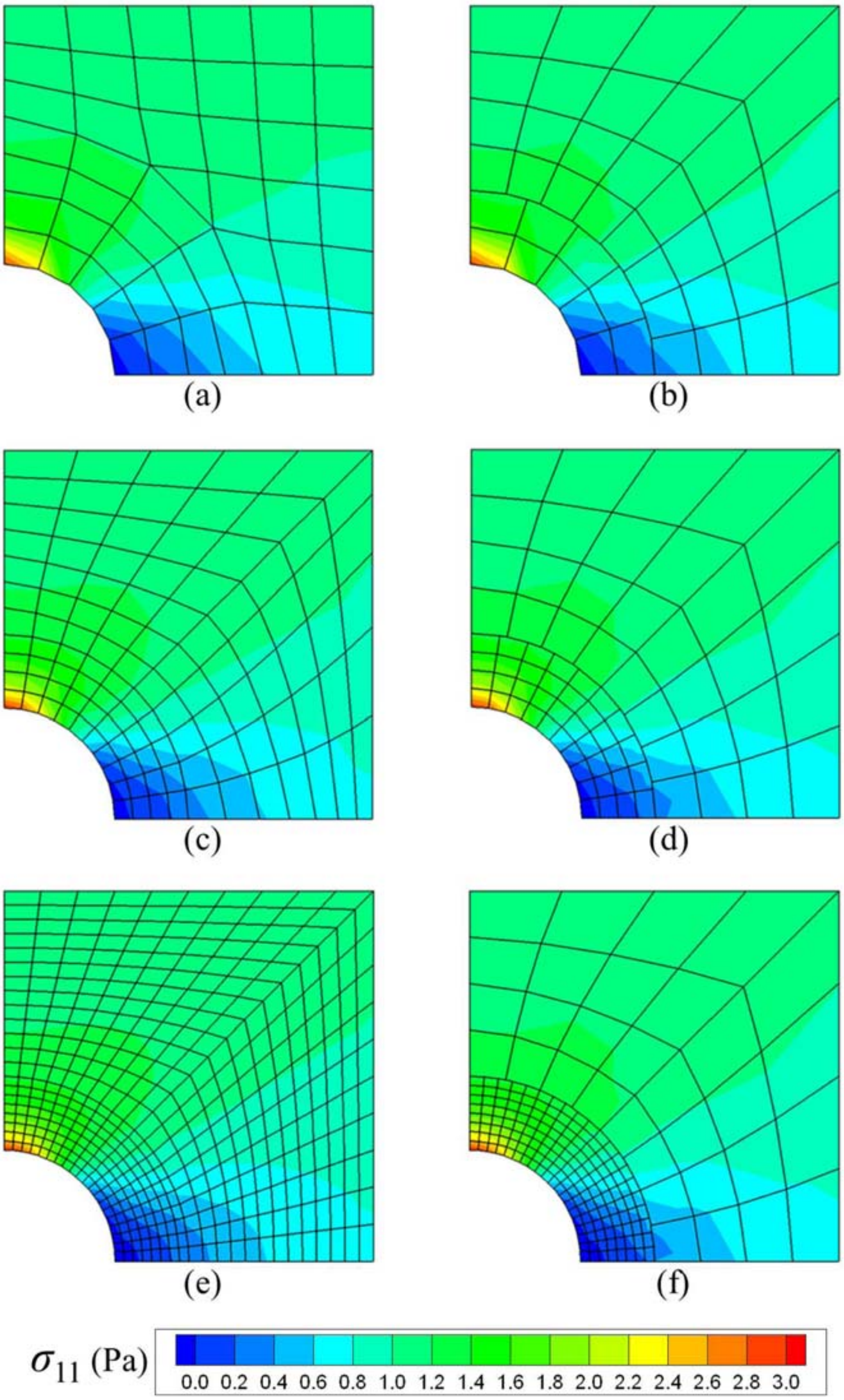

Fig. 10 σ_{11} contour plots of the infinite block including a hole composed of: (a) conventional mesh (64 nodes); (b) mesh with irregular nodes (61 nodes); (c) conventional mesh (132 nodes); (d) mesh with irregular nodes (97 nodes); (e) mesh with conventional elements (462 nodes); (f) mesh with irregular nodes (229 nodes)

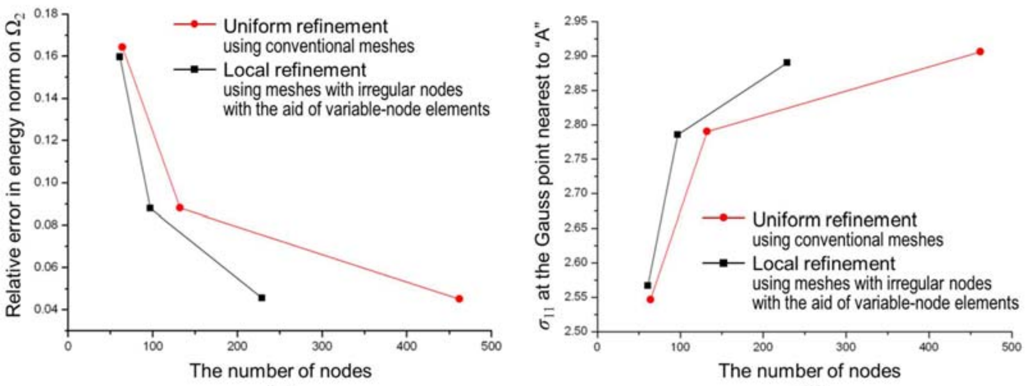

(a) (b)

Fig. 11 Comparison of the results from the conventional meshes and from the locally refined meshes using the variable-node elements with respect to the number of nodes in the infinite block, in terms of: (a) relative error in energy norm on Ω_2; (b) the maximum tensile stress σ_{11} at the Gauss point nearest to "A" in Fig. 9

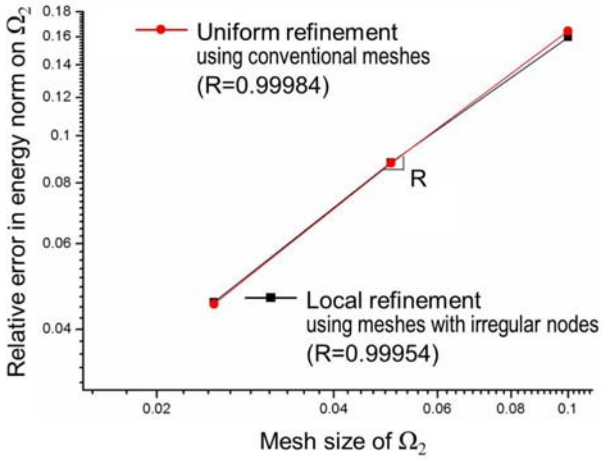

Fig. 12 Comparison of the relative errors in energy norm from the conventional meshes and from the locally refined meshes using the variable-node elements, with respect to mesh size of Ω_2

total number of nodes, comparing the results from the locally refined meshes with those from the conventional meshes. From Fig. 11, we see that the present scheme with the aid of the variable-node elements yields a more rapidly converging solution compared with the conventional mesh case. Furthermore, they still maintain the optimal convergence ratio 1.0 according to the mesh size of Ω_2 as shown in Fig. 12. The aforementioned examples show that our proposed approach is extremely simple as well as accurate, needless to mention that it passes the patch test exactly and also show the consistency of the numerical results even when a curved boundary wherein many irregular nodes are generated.

4.2 Adaptive mesh refinement using variable-node element families

In this subsection, we treat a square plate with point loads and an L-shaped domain. Since these two examples are associated with high stress gradients due to point loads and a wedge, we solve these by using adaptive mesh refinement technique involving many irregular nodes during element subdivision. The irregular nodes in the process of element subdivision are covered by the proposed elements. In addition, we also accommodate a higher level subdivision scheme into the conventional adaptive mesh refinement.

Before considering the last two examples, it will be useful to provide a quick review on adaptive mesh refinement. In making a subdivision of zones containing appreciable error, we employ an error estimator and set a minimum allowable error. We choose the error estimator presented by Zienkiewicz and Zhu (1987) as shown in Eqs. (11) and (12). The error in displacement e_u and the error energy norm $||e||_E$ are represented as follows

$$e_u = u - u_h \tag{11}$$

$$\|e\|_E = \left(\int_\Omega e_u^T L e_u d\Omega\right)^{1/2}$$

$$= \left(\int_\Omega (u-u_h)^T S^T D S (u-u_h) d\Omega\right)^{1/2}$$

$$\left(\int_\Omega (\sigma-\sigma_h)^T D^{-1} (\sigma-\sigma_h) d\Omega\right)^{1/2} \tag{12}$$

where L is the linear elliptic differential operator, D is the elasticity matrix, and S is the strain operator. Furthermore u and u_h are the exact displacement and the approximate displacement from finite element calculation, respectively, and σ and σ_h are the exact and the approximate stress field, respectively. In most engineering problems, the exact displacements u and stresses σ are not known a priori before solution. Zienkiewicz and Zhu (1987) proposed the approximation error measure by using the smoothed stress field σ^* instead of σ.

$$\|e\|_E \cong \|\varepsilon\| = \left(\int_\Omega (\sigma^* - \sigma_h)^T D^{-1} (\sigma^* - \sigma_h) d\Omega\right)^{1/2} \tag{13}$$

$$\|\varepsilon_i\| = \left(\int_{\Omega_i} (\sigma^* - \sigma_h)^T D^{-1} (\sigma^* - \sigma_h) d\Omega_i\right)^{1/2} \tag{14}$$

$$\varepsilon = \sqrt{\sum_{i=1}^{M} \varepsilon_i^2} \tag{15}$$

Note that $\|\varepsilon\|$ and $\|\varepsilon_i\|$ are the approximated strain energy norm in Ω and in the element domain Ω_i, respectively; M is the number of elements. For calculating the stress field σ^* based on σ_h, the global stress smoothing procedure by the least square method is used (Hinton and Campbell 1974). Similar to the error norm $\|\varepsilon\|$, we approximate the exact strain energy norm $\|u\|$ as below

$$\|u\|^2 = \|u_h\|^2 + \|e\|_E^2 \cong \|u_h\|^2 + \varepsilon^2$$

$$\|u\| = \left(\int_\Omega \sigma^T D^{-1} \sigma d\Omega\right)^{1/2}, \quad \|u_h\| = \left(\int_\Omega \sigma_h^T D^{-1} \sigma_h d\Omega\right)^{1/2} \tag{16}$$

Finally, we obtain the relative ratio of the approximated strain energy error norm in the following equation.

$$R = \frac{\|e\|_E}{\|u\|} \times 100(\%) \cong \frac{\varepsilon}{\sqrt{\|u_h\|^2 + \varepsilon^2}} \times 100(\%) \qquad .(17)$$

In the adaptive mesh refinement, we derive the mesh towards a uniform error distribution for all existing elements when a uniform permissible error is prescribed for the entire elements, as in the following equation

$$\|e_o\| = \frac{\|u\|}{\sqrt{M}} \frac{R_o}{100} \cong \left(\frac{\|u_h\|^2 + \varepsilon^2}{M}\right)^{1/2} \frac{R_o}{100} \tag{18}$$

where e_o is the critical error per element in the energy norm, and R_o is the prescribed permissible relative error percentage. As seen in Fig. 13, in order to obtain adaptive meshes yielding a converging solution, we perform several iterations until the stopping criterion is activated.

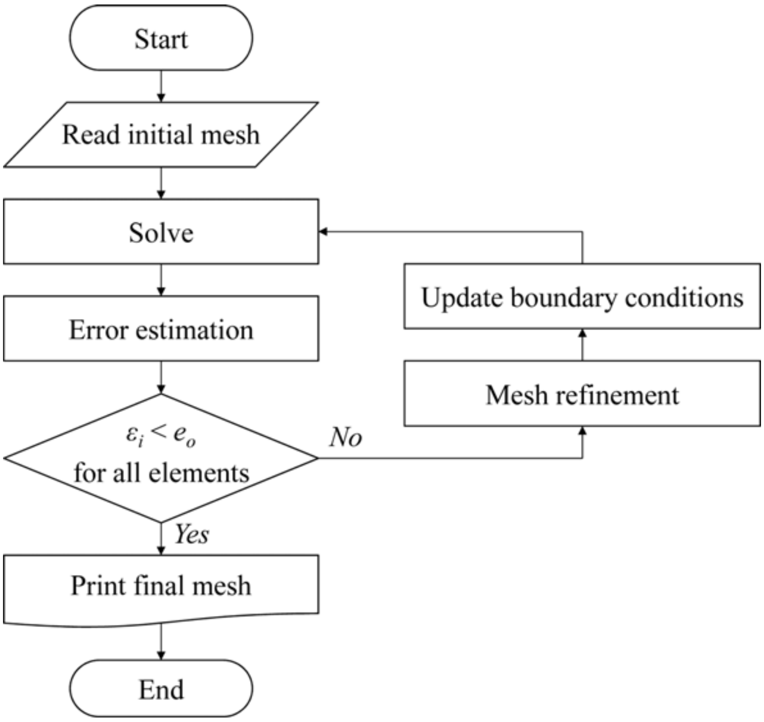

Fig. 13 A procedure of adaptive mesh refinement

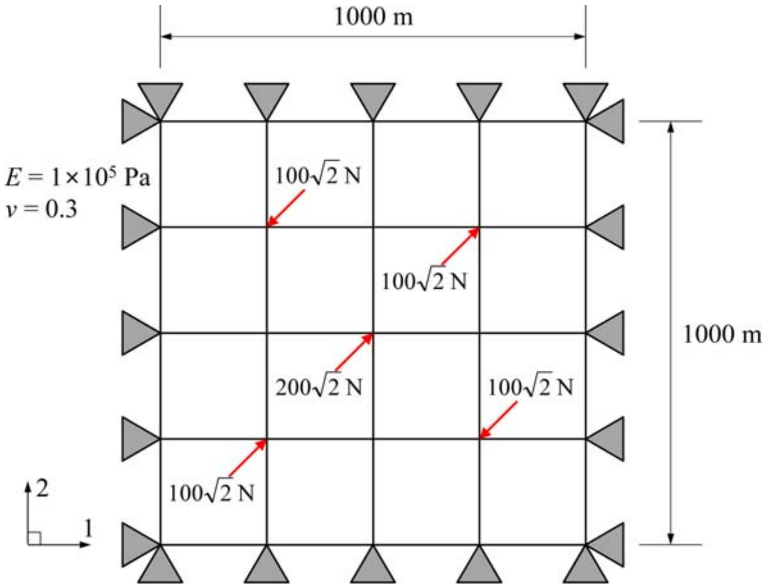

Fig. 14 Geometry and boundary conditions of a square plate under point loads

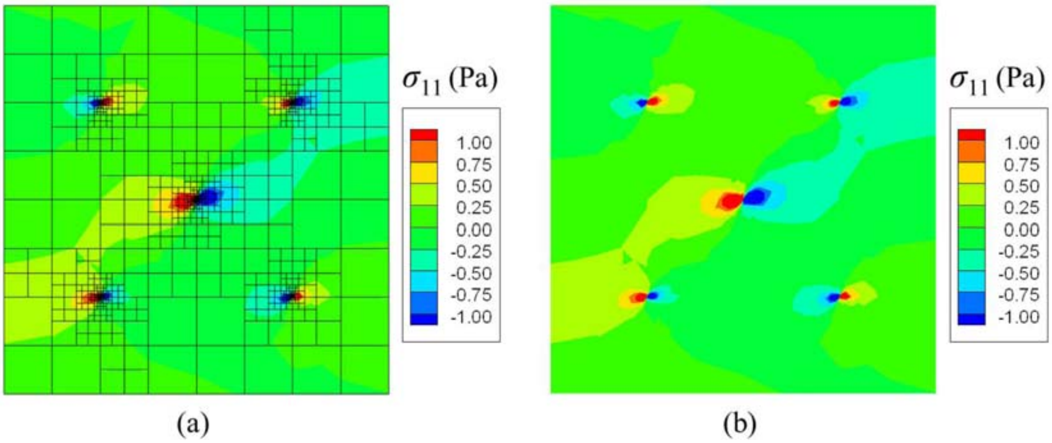

Fig. 15 σ_{11} contour plots of the square plate: (a) with mesh configuration, (b) without mesh configuration

4.2.1 A square plate with point loads with adaptive mesh refinement

Fig. 14 shows a square plate subjected to point loads, initially consisting of 25 nodes and 16 elements. We impose five point loads at the specific positions of the square plate with appropriate boundary conditions, as seen in Fig. 14. Young's modulus and Poisson ratio are 1×10^5 Pa and 0.3, respectively, and plane stress condition is assumed. For the adaptive mesh refinement, we set the relative allowable error R_o to 10%. Through adaptation, we obtain a finite element mesh comprised of 1,775 nodes and 1,426 elements, as seen in Fig. 15. The final mesh configuration is shown in Fig. 16, which is converged in the present adaptation process. Grey color indicates the variable-node elements with two irregular nodes on an element-edge. As already discussed in Section 2, in the

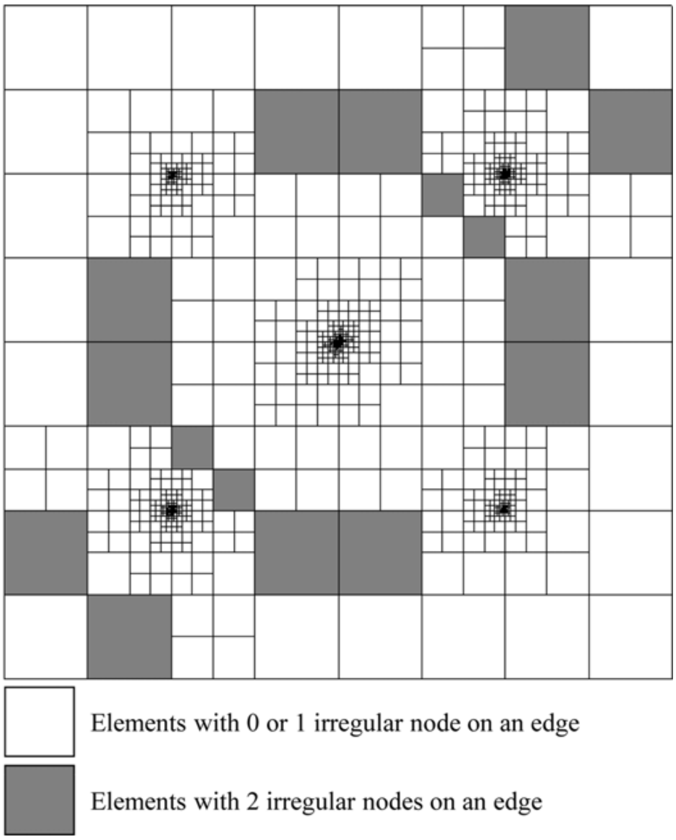

Fig. 16 Converged mesh configuration of the square plate via adaptive mesh refinement with $(4+k+l+m+n)$-node elements

conventional adaptive mesh refinement, we have to perform a sequential remeshing on the grey elements in order to reduce the number of the irregular nodes to 1. However, the present $(4+k+l+m+n)$-node elements makes it possible to avoid any remeshing for the grey elements, as depicted in Fig. 16, in this adaptation procedure.

4.2.2 L-shaped domain with adaptive mesh refinement

The L-shape domain initially consists of a total of 96 nodes and 75 elements with proper boundary conditions, as shown in Fig. 17. In this problem, a high stress gradient takes place at the reentrant corner. Young's modulus is 1×10^7 Pa with Poisson's ratio 0.3, and geometry is described in Fig. 17(a). For adaptive mesh refinement, we set the prescribed allowable error percentage R_o to 0.1%. We solve this problem using two kinds of adaptive mesh refinement techniques: the conventional methodology which splits one element into four bilinear elements, and the higher level subdivision which splits the element into sixteen bilinear elements. We refer to the first technique as subdivision-1 adaptation, and the second as subdivision-2 adaptation for convenience.

We summarize the numerical results according to the adaptation techniques as shown in Fig. 18 and listed in Table 2. It is observed that σ_{11} contour in Fig. 18(a) is in good agreement with that in Fig. 18(b). However, the convergence behaviors are quite different, as listed in Table 2. The

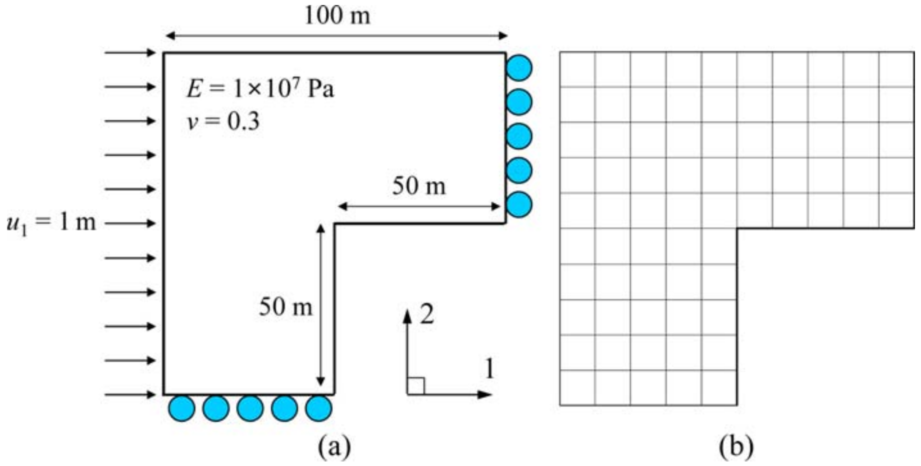

Fig. 17 Schematic view of an L-shaped domain: (a) geometry and boundary conditions, (b) initial mesh configuration

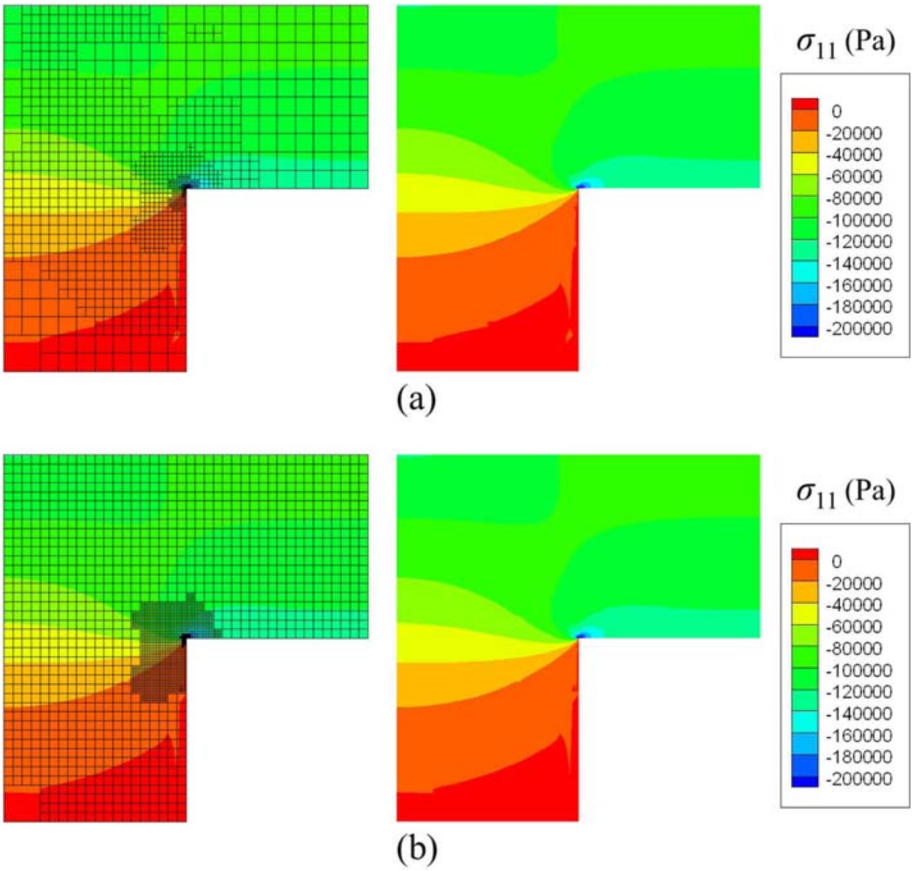

Fig. 18 σ_{11} contour plots of the L-shaped domain with and without mesh configuration using: (a) subdivision-1 adaptation, (b) subdivision-2 adaptation

Table 2 Iteration count and number of nodes by subdivision-1 and subdivision-2 adaptation

Iteration count	Number of nodes	
	Subdivision-1 adaptation	Subdivision-2 adaptation
1	96	96
2	338	1,266
3	853	2,400
4	1,092	2,673
5	1,207	2,766 (converged)
6	1,266	
7	1,305	
8	1,326	
9	1,331 (converged)	

subdivision-1 adaptation takes 9 iterations and ends up with 1,331 nodes, On the other hand, the subdivision-2 adaptation needs 5 iterations and leads 2,766 nodes. The use of a proper combination of subdivision-1 adaptation with subdivision-2 adaptation might be the optimal approach for every class of problems. We leave this, however, as future work. It is noted that 1-irregular node rule-free adaptive mesh computation can be successfully achieved with the aid of the variable-node elements.

5. Conclusions

In this paper, we have reported the variable-node finite element families using the point interpolation, termed the $(4+k+l+m+n)$-node elements, which accommodate an arbitrary number of nodes (k, l, m, and n) on each element-edge. For the construction of their shape functions, we employ the point interpolation and a set of special polynomial bases containing the slope discontinuities. These elements only require the 2×2 Gauss integration per element subdomain, because their shape functions retain the bilinear interpolation property within each subdomain. Although they have many irregular nodes or side nodes, their shape functions are integrated properly by subdomain-wise Gauss integration, as verified by several benchmark problems. Their generality and strong potential in resolving nonmatching mesh problems have been illustrated through several examples, which appear in adaptive mesh refinement problems by relaxing the 1-irregular node rule with the aid of variable-node element families. The extension to three dimensional solid elements and shell elements with the variable number of nodes, and to nonlinear problems are currently ongoing, and will be reported when completed.

Acknowledgements

The corresponding author gratefully acknowledges the support from the National Research Foundation of Korea (NRF) Grant funded by the Korean Government (MEST) (R0A-2007-000-20115-0).

References

Aminpour, M.A., Ransom, J.B. and McCleary, S.L. (1995), "A coupled analysis method for structures with independently modeled finite element sub-domains", *Int. J. Numer. Meth. Eng.*, **38**, 3695-3718.

Cho, Y.S., Jun, S., Im, S. and Kim, H.G. (2005), "An improved interface element with variable nodes for non-matching finite element meshes", *Comput. Meth. Appl. Mech. Eng.*, **194**, 3022-3046.

Cho, Y.S. and Im, S. (2006a), "MLS-based variable-node elements compatible with quadratic interpolation Part I: formulation and application for non-matching meshes", *Int. J. Numer. Meth. Eng.*, **65**, 494-516.

Cho, Y.S. and Im, S. (2006b), "MLS-based variable-node elements compatible with quadratic interpolation Part II: application for finite crack element", *Int. J. Numer. Meth. Eng.*, **65**, 517-547.

Choi, C.K. and Lee, N.H. (1993), "Three dimensional transition solid elements for adaptive mesh gradation", *Struct. Eng. Mech.*, **1**, 61-74.

Choi, C.K. and Lee, N.H. (1996), "A 3-D adaptive mesh refinement using variable-node solid transition elements", *Int. J. Numer. Meth. Eng.*, **39**, 1585-1606.

Choi, C.K., Lee, E.J. and Yu, W.J. (2004), "Adaptive mesh refinement/recovery strategy for FEA", *Struct. Eng. Mech.*, **17**, 379-391.

Choi, C.K. and Park, Y-M. (1992), "An adaptive h-refinement using transition element for plate bending problems", *Int. J. Numer. Meth. Eng.*, **35**, 145-163.

Christie, I. and Hall, C. (1984), "The maximum principle for bilinear elements", *Int. J. Numer. Meth. Eng.*, **20**, 549-553.

Flemisch, B., Puso, M.A. and Wohlmuth, B.I. (2005), "A new dual mortar method for curved interfaces: 2D elasticity", *Int. J. Numer. Meth. Eng.*, **63**, 813-832.

Floater, M.S. (2003), "Mean value coordinates", *Comput. Aid. Geom. Des.*, **20**, 19-27.

Gupta, A.K. (1978), "A finite element for transition from a fine to a coarse grid", *Int. J. Numer. Meth. Eng.*, **12**, 35-45.

Hinton, E. and Campbell, J.S. (1974), "Local and global smoothing of discontinuous finite element function using a least square method", *Int. J. Numer. Meth. Eng.*, **8**, 461-480.

Hughes, T.J.R. (1989), *The Finite Element Method: Linear Static and Dynamics Finite Element Analysis*, Prentice Hall: Englewood Cliffs, NJ.

Kim, H.G. (2002), "Interface element method (IEM) for a partitioned system with non-matching interfaces", *Comput. Meth. Appl. Mech. Eng.*, **191**, 3165-3194.

Kim, H.G. (2008), "Development of three-dimensional interface elements for coupling of non-matching hexahedral meshes", *Comput. Meth. Appl. Mech. Eng.*, **197**, 3870-3882.

Kim, J.H., Lim, J.H., Lee, J.H. and Im, S. (2008), "A new computational approach to contact mechanics using variable-node finite elements", *Int. J. Numer. Meth. Eng.*, **73**, 1966-1988.

Lim, J.H. and Im, S. (2007), "(4 + n)-noded moving least square (MLS)-based finite elements for mesh gradation", *Struct. Eng. Mech.*, **25**, 91-106.

Lim, J.H., Im, S. and Cho, Y.S. (2007a), "MLS (moving least square)-based finite elements for three-dimensional nonmatching meshes and adaptive mesh refinement", *Comput. Meth. Appl. Mech. Eng.*, **196**, 2216-2228.

Lim, J.H., Im, S. and Cho, Y.S. (2007b), "Variable-node elements for nonmatching meshes by means of MLS (moving least-square) scheme", *Int. J. Numer. Meth. Eng.*, **72**, 835-857.

Lim, J.H., Sohn, D., Lee, J.H. and Im, S. (2010), "Variable-node finite elements with smoothed integration techniques and their applications for multiscale mechanics problems", *Comput. Struct.*, **88**, 413-425.

Liu, G.R., Dai, K.Y. and Nguyen, T.T. (2007), "A smoothed finite element method for mechanics problems", *Comput. Mech.*, **39**, 859-877.

Lo, S.H., Wan, K.H. and Sze, K.Y. (2006), "Adaptive refinement analysis using hybrid-stress transition elements", *Comput. Struct.*, **84**, 2212-2230.

Lo, S.H., Wu, D. and Sze, K.Y. (2010), "Adaptive meshing and analysis using transitional quadrilateral and hexahedral elements", *Finite Elem. Anal. Des.*, **46**, 2-16.

Nguyen-Thoi, T., Liu, G.R. and Nguyen-Xuan, H. (2011), "An n-sided polygonal edge-based smoothed finite element method (nES-FEM) for solid mechanics", *Int. J. Numer. Meth. Eng.*, **27**, 1446-1472.

Park, K.C., Felippa, C.A. and Rebel, G. (2002), "A simple algorithm for localized construction of non-matching structural interfaces", *Int. J. Numer. Meth. Eng.*, **53**, 2117-2142.

Puso, M.A. (2004), "A 3D mortar method for solid mechanics", *Int. J. Numer. Meth. Eng.*, **59**, 315-336.

Sohn, D., Cho, Y.S. and Im, S. (2012), "A novel scheme to generate meshes with hexahedral elements and poly-pyramid elements: The carving technique", *Comput. Meth. Appl. Mech. Eng.*, **201-204**, 208-227.

Sohn, D., Lim, J.H., Cho, Y.S., Kim, J.H. and Im, S. (2011), "Finite element analysis of quasistatic crack propagation in brittle media with voids or inclusions", *J. Comput. Phys.*, **230**, 6866-6899.

Timoshenko, S.P. and Goodier, J.N. (1970), *Theory of Elasticity*, McGraw-Hill, NY.

Varga, R.S. (1966), "On a discrete maximum principle", *SIAM J. Numer. Anal.*, **3**, 355-359.

Wachspress, E.L. (1975), *A Rational Finite Element Basis*, Academic press, NY.

Wu, D., Sze, K.Y. and Lo, S.H. (2008), "Two- and three-dimensional transition elements for adaptive mesh refinement analysis of elasticity problems", *Int. J. Numer. Meth. Eng.*, **78**, 587-630.

Zienkiewicz, O.C. and Zhu, J.Z. (1987), "A simple error estimator and adaptive procedure for practical engineering analysis", *Int. J. Numer. Meth. Eng.*, **24**, 337-357.